2R.5

DOPPLER RADAR AND PROFILER OBSERVATIONS OF BOUNDARY EVOLUTION AND COLLISION

Haldun Karan and Kevin R. Knupp
University of Alabama in Huntsville
Huntsville, Alabama

1. INTRODUCTION

Boundary collisions (Wakimoto and Kingsmill 1995; Kingsmill and Crook 2003) have gained attentions because of their role on forming gravity waves, generating additional lifting of air to the *LCL* and even *LFC* and forming deep cumulus and further to initiate convection, or simply strengthening existence storm cells. Wilson and Schreiber (1986) examined storm initiation locations with respect to boundary convergence zones. They found that 95% (≥ 60 dBZ_e) of the 418 storms were initiated in close proximity to radar finelines. They also observed that colliding convergence lines initiated new storms or intensified existing storms in 71% of the cases. Kingsmill and Crook (2003) found that seven of 10 gust front-sea breeze collision cases produced dual boundaries after collisions, and 70% of them initiated new convection or enhanced existing convection. Yet, Kingsmill (1995), after examining gust front-sea breeze collision, did not observe any enhancement in convection associated with boundary collision.

2. ABL CHARACTERISTICS AND OVERVIEW OF BOUNDARIES

The current study investigates a collision of two outflow boundaries emanated from thunderstorms west and east of the WSR-88D Sioux Falls radar. The observation took place during the BAMEX, Bow Echo and MCV Experiment, between June 16 and June 17, 2003. A map of isochrones of the two gust fronts from 2200 to 2345 UTC on 16 June 2003 is shown in Fig. 1 (LST=UTC-5 hour). The figure also depicts locations of some of the ASOS/AWOS surface stations, KFSD radar side, and locations of the MGLASS sounding unit and the MIPS (Mobile Integrated Profiling System). The eastward moving boundary (B1, dashed line) formed 100 km west of the KFSD radar around 2145 UTC, and had an average speed of 11.5 ms^{-1} between 2200 and 2345 UTC time interval. The westward moving boundary (B2), on the other hand, was an old, slow moving gust front. It formed 60 km east of the KFSD radar at 1845 UTC. Average propagation speed of B2 within the same time period was 4.2 ms^{-1}, much slower than its counterpart.

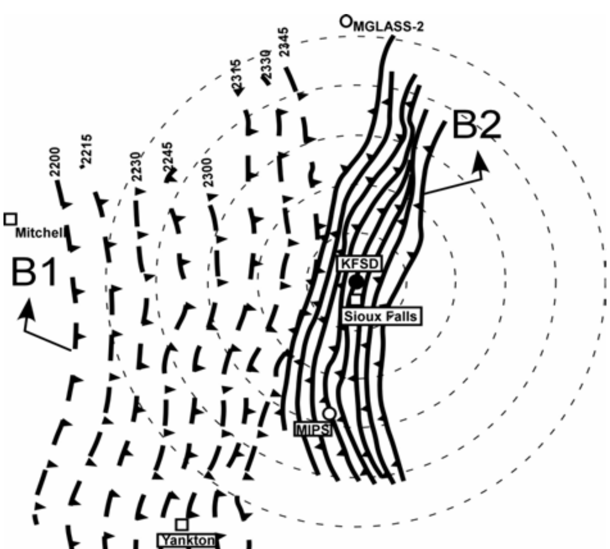

Fig.1. Isochrone analysis of boundary 1-dashed (boundary 2-solid) moving eastward (westward). Distance between each ring is 15 km. Boundary collision time is about 2345 UTC (1845 CST).

Prominent features of low level atmospheric conditions are weak water vapor and warm air advection from the south into the study area. The 850 mb flow at 1200 UTC (not shown) also suggested a large scale convergent region over Nebraska and South Dakota. An MGLASS-2 sounding at 2235 UTC (not shown) indicated well mixed CBL extending up to 2.4 km. Horizontal convective rolls (*HCR*) can easily be distinguished by radar finelines in Fig. 2. Radar reflectivity bands, varying between 0 and 10 dBZ, are shown to be consequence of convergence associated with organized convective circulations within horizontal roll vortices (Fankhauser et al. 1995). As suggested by both the MGLASS-2 sounding at 2235 UTC, and KFSD VAD (velocity-azimuth display, not shown), *HCR* orientations were similar to the low

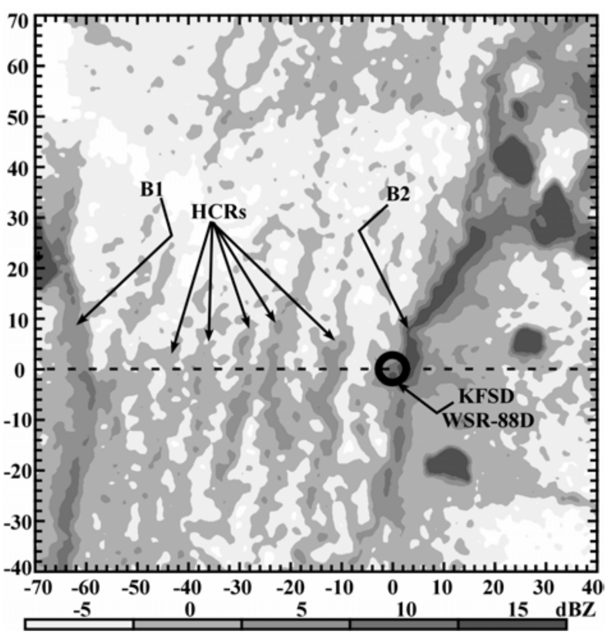

Fig. 2. Sioux Falls, SD WSR-88D radar reflectivity factor at 1 km AGL at 2235 UTC. The figure also depicts eastward moving boundary (B1), slow westward moving boundary (B2), and some radar fine lines, indicative of roll circulations, varying from 0 dBZ to 10 dBZ.

level wind and shear direction, and well aligned parallel to the two boundaries. North-northeast to south-southwest oriented enhanced values of reflectivity factors existed between the two boundaries before the collision. Boundary B1 systematically encountered roll updrafts and downdrafts as it propagated to the East.

Both boundaries individually initiated new convective cells of 50-55 dBZ intensity as they approached and collided with each other (Fig. 3a-b). During and after the collision (Fig. 3b-d), new cells were initiated along the collision line. Interestingly, convection was not initiated close to the collision point (Fig. 3b-c). Rather, intense convection occurred, or storm cell strength was enhanced, 30-40 km south and north of along-collision boundary axis. After the collision (Fig. 3c-d), AC_{B2} appears to have gravity wave type disturbances having two waves with two major updrafts indicated by two distinct radar finelines in Fig. 3d. A storm system 30 km southwest of KFSD radar (Fig. 3c) formed new gust fronts that propagated to the northwest and east-northeast. The east-northeast moving gust front (Fig. 3d) lifted the AC_{B1} boundary. The *MIPS* profiler observed both, an elevated gust fronts labeled AC_{B1} at 2-2.5 km AGL, and near surface gust front, as they passed over the *MIPS.*

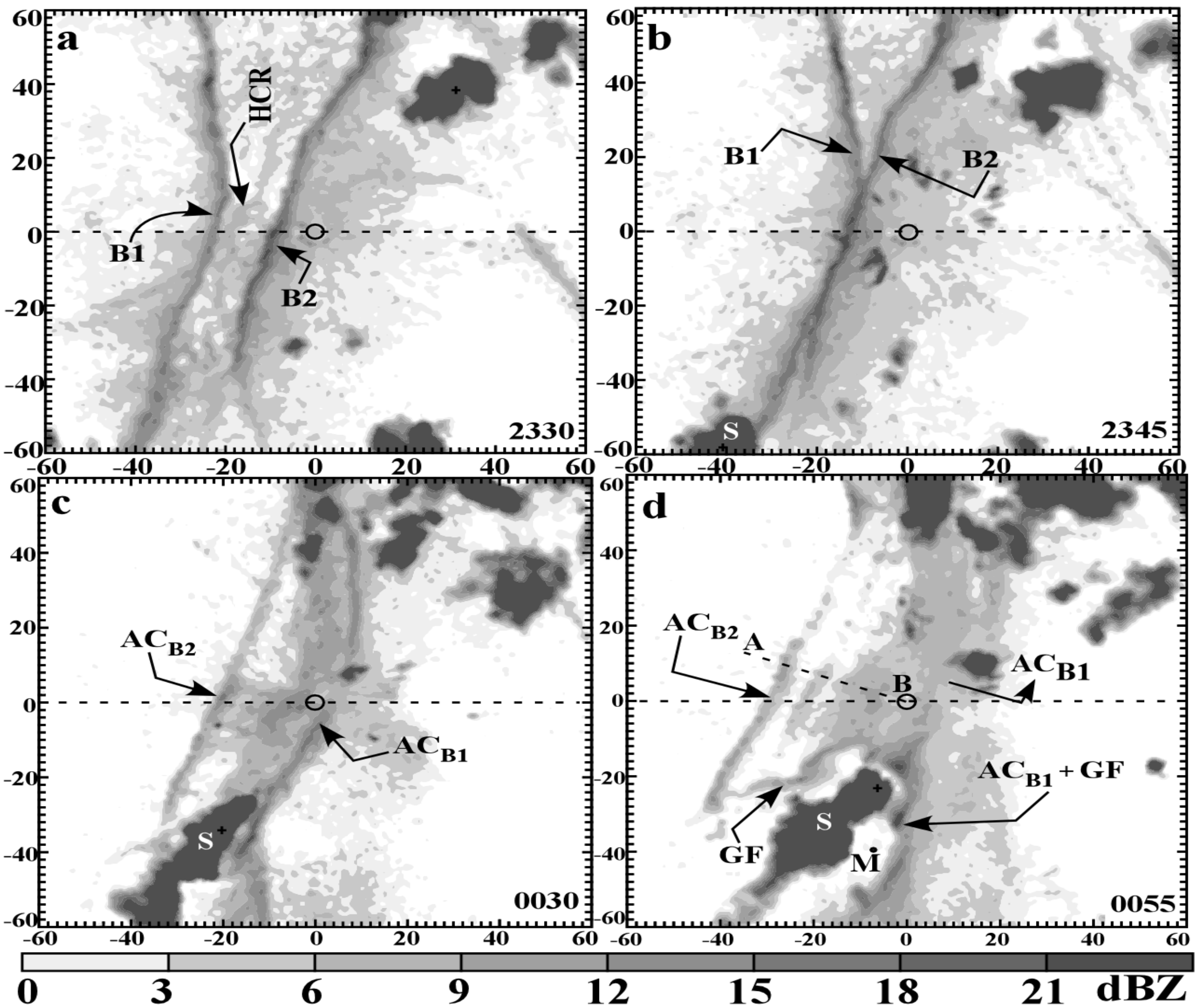

Fig. 3. Sioux Fall, SD WSR-88D reflectivity factor on X-Y plane at 0.5 km AGL at a) 2330, b) 2345 on 16 June and c) 0030 and d) 0055 UTC on 17 June, 2003. A circle with letter M depicts the MIPS location.

3. KINEMATIC AND THERMODYNAMIC STRUCTURES OF THE BOUNDARIES

3.1 PRE-COLLISION

Surface observations acquired from Mitchell and Sioux Falls revealed that outflow air behind boundary B1 was colder and moister than the B2 outflow. One of the most widely used methods to investigate similarities between atmospheric boundaries and laboratory generated density currents is the internal Froude number, Fr (ratio of inertial force to force of gravity). The following sets of equations are used to investigate the similarities between observed outflow boundaries and density currents.

$$Fr = \frac{\overline{C}_{BND} - b\overline{UA}}{\sqrt{g'h}},$$

where $\overline{C}_{BND}$ and $\overline{UA}$ are average propagation speed of the boundary, mean ground relative ambient flow ahead of and perpendicular to the boundary, g' is a reduced gravity determined from the following relationship:

$$g' = g\frac{\overline{\theta}_{v-env} - \overline{\theta}_{v-cold}}{\overline{\theta}_{v-cold}}$$

Boundary propagation speed is also tested with the following relationship:

$$V = Fr\left(\Delta P \big/ \rho_w\right)^{1/2}$$

Using radar fine line (isochrones), surface, and sounding information, Fr number is found to be about 1.3 close to theoretical upper limit of √2 (Benjamin 1968).

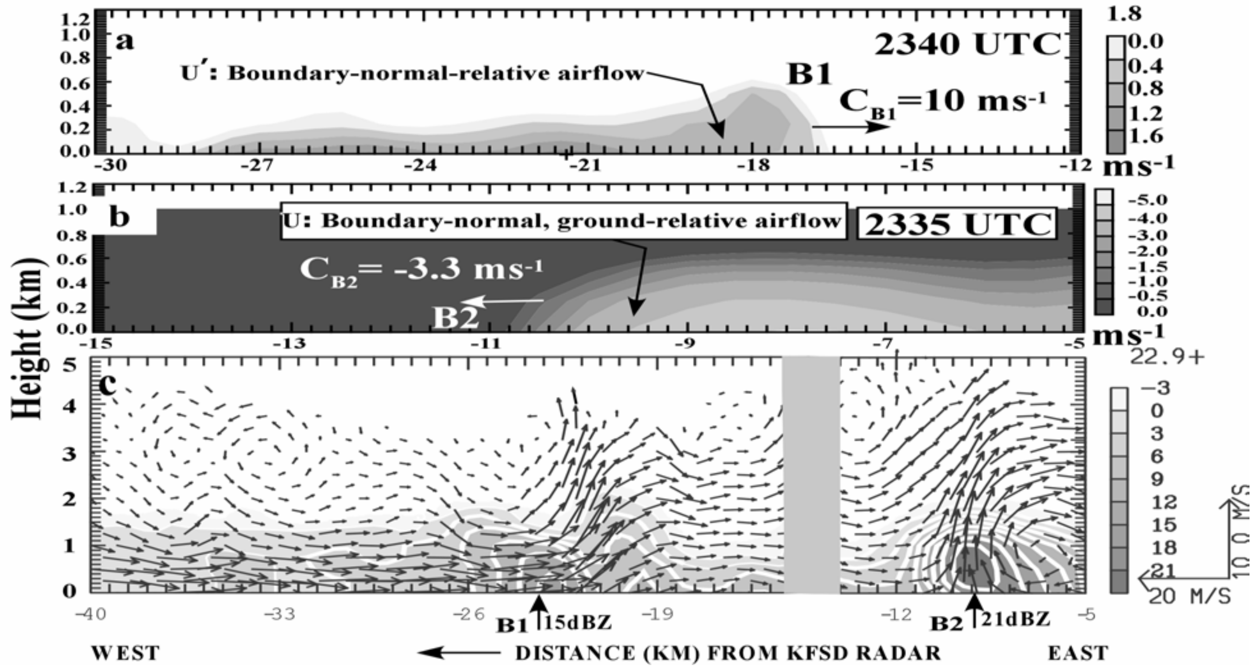

Fig. 4. Vertical structures of B1 and B2. C_{B1} and C_{B2} are propagation speeds of the B1 and B2 boundaries, respectively. a) Eastward moving boundary. U′ is B1-relative airflow normal to the boundary. Shaded areas show higher airflow behind the B1 reaching maximum values of 1.8 ms^{-1}. b) Westward moving boundary. U is the ground-relative airflow behind the B2. Negative values (light grey) indicate that flow is easterly. c) *u-w* component of ground-relative flow at 2330 UTC. Shaded region with overlaid contours displays reflectivity factor *Z*. Locations of the maximum *Zs* associated with both boundaries are indicated by arrows with values. The region shown as a grey column in (c) is to separate two regions: Radial velocity and *Z* fields are advected by average speed of B1 (10ms^{-1}) starting at x=-14 km. No advection is applied between -5 km and -14 km.

Since both boundaries exhibited approximately east-west directional propagation close to the KFSD radar, we constructed east-west component of the flow (*u* component) by assuming radial velocities to be true *u* component of the flow. The vertical wind component was calculated using the two-dimensional equation of continuity assuming north-sound component of the wind is uniform. Since B1 was a fast moving boundary (~10 ms^{-1}), both reflectivity and radial velocity fields are advected toward the west with height starting at x= -14 km.

Both boundaries slowed down before the collision took place. B1 clearly shows an elevated head structure extending up to 600 m AGL, near a factor of two higher than the body height (Fig. 4a). *U′* is the excess speed of the flow behind B1, indicative of mass transport. B2 was moving 3.3 ms^{-1}, much slower than its counterpart, and its outflow speed was less than the boundary propagation speed *(U′*≅0 ms^{-1}) (Fig. 4b). An HCR just ahead of B1 (x = -19 km) resulted in pseudo dual reflectivity maxima. The reflectivity field associated with B1 is tilted back toward the west with height even though flow field at the leading edge of B1 tilted forward (Fig. 4c).

Both boundaries were associated with 5−5.5 ms^{-1} updrafts. Convergence with maximum values of $-3-4\times10^{-3}$ s^{-1} was analyzed in the lowest 1 km. Updrafts diverge and weaken above that level. Unlike B1, B2 exhibited a much steeper updraft structure. Return flow above the heads of the gust fronts exhibited distinct difference. Westerly flow above the head of B2 is much more distinguishable and located just above 1 km AGL. Due to the opposing ambient flow, vertical displacements of air flow associated with B2 started closer to the surface. The ambient wind profile seems to have a major role on the regulating flow characteristics at the interface between the outflow and ambient flow above (consistent with number of simulations of Rotunno 1988). Even though B1 is a much colder and faster propagating boundary, return flow associated with B2 is more prominent. Radar echoes associated with B2 also had higher values (~21 dBZ_e). This could be explained by the fact that B2 is a slow moving boundary and that would increase collection time of biological fliers and/or dust particles within the convergence zone. Convergence line of the B1 was almost three times faster than its counterpart. Scattering particulates would have less time to be collected within the convergent line.

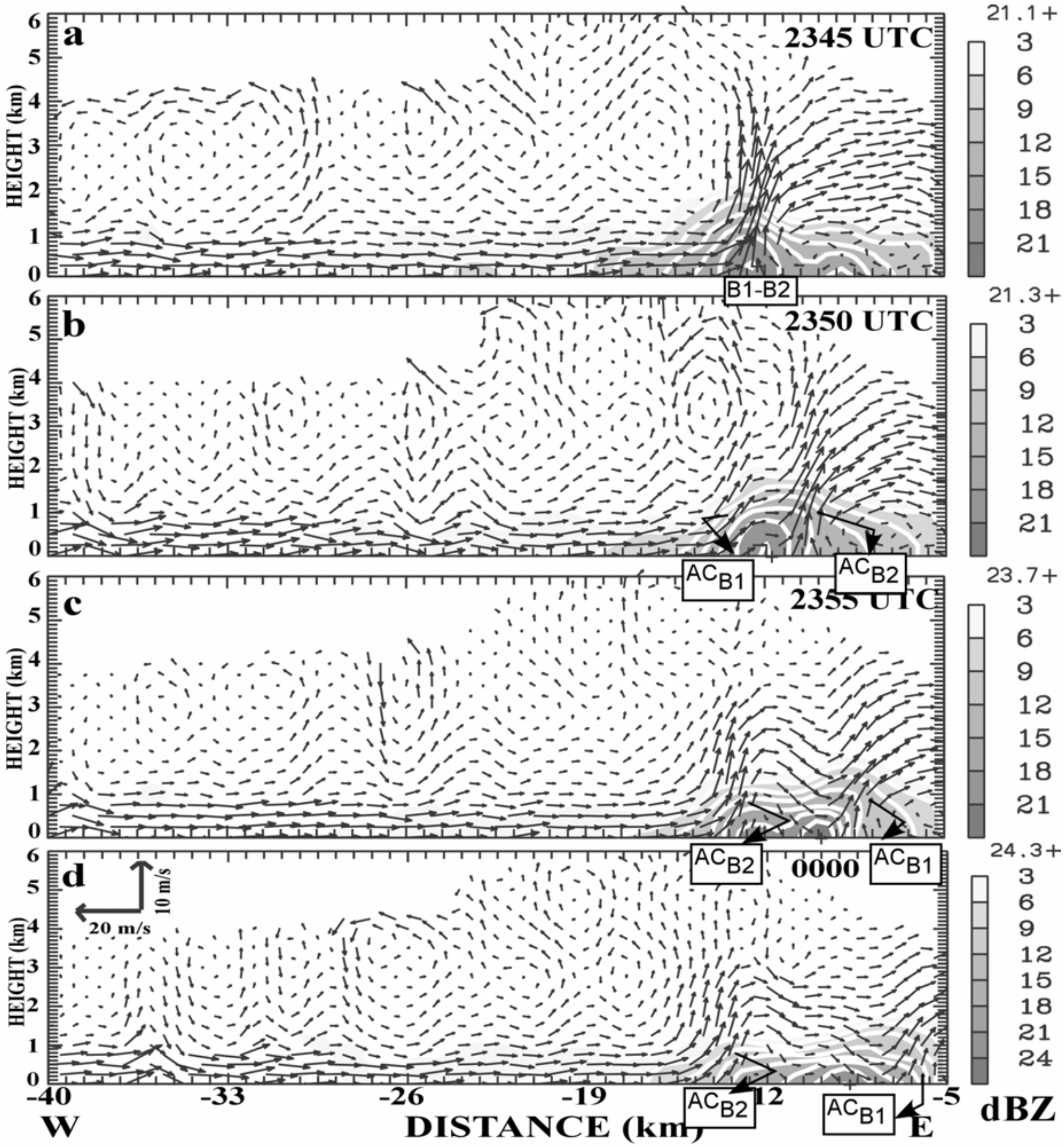

Fig. 5. U-W component of the flow at a) 2345 b) 2350 c) 2355, d) 0000 UTC. No advection is applied to reflectivity and radial velocity fields

3.2 DURING THE COLLISION

East-west (u) and vertical (w) components of the flow field during and shortly after the collision were constructed by assuming that outflows are perpendicular to their parent gust fronts (Fig. 5). The outflow ($u \sim 12$ ms^{-1}) associated with B1 dominated the lowest 0.8 km and collided with the outflow of B2 (-4 ms^{-1}) near x = -12.5 km. The convergent zone ($Z_e \geq 10$ dBZ$_e$**)** became wider, covering the distance between x = -7 km and x = -15.5 km. Maximum reflectivity factor and vertical velocities are 21.1 dBZ$_e$ and 10.5 ms^{-1}, respectively (Fig. 5a). Updrafts attained maximum values (w_{max}=10.5 ms^{-1}) and extended up to 5 km AGL, while strongest vertical velocity core ($w \geq 3$ ms^{-1}) dominated from surface up to 4 km AGL. Reflectivity values greater than 9 dBZ$_e$ reached maximum heights at the collision time at 2345 UTC (z ≈ 1.7 km). Convergence with maximum values of -3×10^{-3} s^{-1} remained within the lowest 1 km. Return flow above the heads of the gust fronts exhibited a distinct difference. An easterly return flow for B1 occurred at above 4 km AGL, while a westerly return flow for B2 took place at 1 km AGL.

As seen in Fig.5b, the convergent zone, is displaced about 1 km east of the Z maximum. Vertical velocity fields exhibited two maxima, one centered at x ≈ -10.6 km with w_{max} of 7.2 ms^{-1} and the other at x ≈ -13.4 km with w_{max} of 4 ms^{-1}.

Knowing that the B2 updraft is much steeper and slightly higher, we speculate that the updraft located at x ≈ -10.6 km is associated with B2. There is also an increase in easterly flow above the B1 updrafts. Warmer ambient air and cooler B2 outflow may have crossed toward the west above B1 since B1 had colder (denser) air than B2 outflows. Moreover, since the Z_e maximum core was pushed toward the east, the B1 outflow, at the first impact, may have pushed the B2 boundary toward the east as well. Easterly return flow at and above 4 km AGL and downdrafts (x ≈ -15.5 km) associated with the return flow caused two convergence maxima behind B1 updrafts (not shown). Comparison of convergence zones revealed that B2 had slightly greater and much wider (coverage) convergent zone at this time.

Two separate updrafts with dual Z_e maxima formed 10 minutes after the collision (Fig. 5c). AC_{B2} displayed steep updraft like its predecessor B2 with 6.2 ms^{-1} vertical velocity maximum (x = -12.7 km). A main difference between AC_{B2} and B2 is that updrafts associated with AC_{B2} dominates 0-2 km layer, shallower than B2 updrafts. The AC_{B1} updraft exhibits a similar eastward tilt as the B1 updraft (see Fig. 5c), but are much shallower. The two updrafts are separated with downdrafts reaching up to -2 ms^{-1} near x ≈ -10.0 km. This downdraft caused near surface divergence (3×10^{-3} s^{-1}, not shown), and helped to enhance Z_e values ($Z_{e\text{-}max}$ = 23.7 dBZ_e). Interestingly, highest Z_e values did not occur where the greater convergence was present. The convergence zone associated with AC_{B1} (x ≈ -8.5 km, not shown) occurred about 1.5-2 km east of the highest Z_e values. Downdrafts may have brought scattering particles behind AC_{B1}, and also enhanced Bragg scattering by supplying an air mass with different thermodynamic characteristics (drier, and colder perhaps).

AC_{B1} appears to move faster than AC_{B2} during the period between 2345-0000 UTC (Fig. 5d). The reflectivity field associated with both boundaries strengthened and became more flat, and higher Z_e values were between the two updrafts. The updrafts also became a bit shallower by this time. The maximum vertical velocities associated with AC_{B2} and AC_{B1} were about 4.8 ms^{-1} and 3.5 ms^{-1}, respectively. Updraft-downdraft couplets, for both AC_{B2} and AC_{B1} have already been established. Downdrafts of AC_{B2} and AC_{B1} are centered at x = -12 km and -9 km, respectively. Divergence (not shown) between the two updrafts weakened but became broader. Radial velocity observations alone (not shown) suggested that outbound (positive-away from the radar) flow associated with B2 boundary first is observed at 2355 UTC between 0.4-0.8 km layers. This elevated, westward directed flow above descended behind the AC_{B1} boundary, and became a density current.

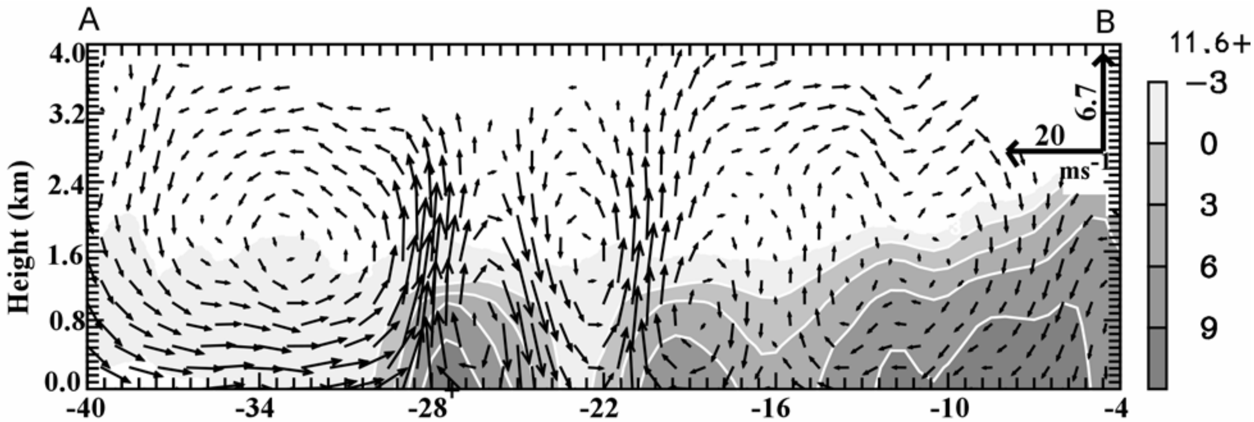

Fig. 6. U-W field overlaid on Z_e along the A-B cross-section shown at Fig. 3d at 0055 UTC on 16 June, 2003. The Z_e and radial velocity fields are advected toward the east.

3.3 AFTER COLLISION — B2

AC_{B2} began as an intrusion flow above B1 soon after the collision, and within 10-15 min, AC_{B2} was located behind AC_{B1}, moving in the opposite direction, resembled a gravity current structure. In the last phase, the system circulation associated with AC_{B2} formed gravity wave circulations behind the boundary (Fig. 6). Numerical and laboratory simulations and observational studies of density currents, particularly gust fronts, show horizontal vortices forming behind the gust front (Droegemeier and Wilhelmson 1987, Xue 2002, Simpson and Britter 1980). Maximum westerly ambient flow and maximum easterly AC_{B2} outflow were calculated to be about 7 ms^{-1} and -4 ms^{-1}, respectively. Therefore, it was not a pure gravity current but rather the system resembled a hybrid gravity current and gravity wave system. Westerly flow was forced upward by the AC_{B2} updrafts (reaching up to 6.3 ms^{-1}), and gained negative buoyancy. In return, a downward motion followed. Thus, the disturbed air mass exhibited a wave structure behind the gravity wave/current hybrid as seen by dual outbound radial velocity field (not shown) and dual radar finelines in Fig. 3d. Radial velocity field indicated 3 ms^{-1} westerly flow above the AC_{B2} head. Average easterly flow of 3 ms^{-1} associated with AC_{B2} created significant velocity shear between the two media. Considering that the gravity current (AC_{B2}) was rather shallow and moved in a stable layer any vortices (either due to the hydrostatic or K-H instability or both) formed behind the boundary head could reach to the surface and create its own surface divergence/convergence regions. This process could separate gust frontal head from its body and form wave structure seen at Figure 6.

3.4 AFTER COLLISION — B1

Convective initiation and subsequent strengthening of cells along B1, south-west of the radar, are shown in Fig.3. While AC_{B1} continued to move eastward, a new outflow emanated from storm “S” was formed around 0025 UTC. This can be seen in Fig. 3 c-d, where enhanced reflectivity factors are spreading away from the storm with an arch shape way in both east and north-west of the storm. The MIPS sampled the outflow boundary (labeled GF) moving eastward, and also AC_{B1} passage was sampled about the time with GF passage by the MIPS.

AC_{B1} and GF passed over Sioux Falls, Pavilion SD surface station (not shown). The temperature and mixing ratio showed no variations associated with AC_{B1} passage. On the other hand, southerly 4-6 ms^{-1} flow changed to south-southwesterly with weak flow (~2-3 ms^{-1}). The wind direction shift was not temporary (suggestive to gravity wave passage) but rather sustained. As the GF passed the same station at 0115 UTC, the temperature (mixing ratio) decreased (increased) and surface wind speed increased from 2 ms^{-1} to 8 ms^{-1}, showing signs of density current type flow. It appears that AC_{B1} was not a pure density current since it was not associated with mass transport. After the collision, this boundary weakened but still had a circulation intact with the surface.

Convergent boundary zone (*CBZ*) is defined as a region where its leading edge starts with minimum surface wind speed and beginning of pressure increase, indicative of near surface convergent flows (Fig. 7). Wind directional change occurred within the *CBZ* (suggesting a transition or turbulent zone). Maximum surface winds of 15 ms^{-1}, ~3 ms^{-1} excess of boundary propagation speed, marked the end of the *CBZ*. Based on surface observations alone, *CBZ* occurred between shortly after 0041 and 0049 UTC. Pressure and virtual potential temperature within the CBZ varied for 0.64 mb and 1.4 K, respectively. Dynamic pressure as seen at Fig. 7, was a dominant factor in pressure rise such that pressure jumped for 0.36 mb at 0044 UTC, yet subsequent increase of 0.28 mb was associated with hydrostatic pressure. Using Bernoulli’s principle, computed dynamic pressure was found to be 0.38 mb, close agreement with observed non-hydrostatic pressure jump of 0.36 mb at 0044 UTC.

AC_{B1} had already passed over the MIPS few minutes before the MIPS observations started. *MIPS* profiler observations between 0037 and 0133 UTC are shown in Fig. 8a-b. The 915 MHz profiler sampled an updraft-downdraft circulation associated with the GF passage and an elevated boundary passage, AC_{B1}. Careful analysis between the surface observations and 1-min profiler mean vertical velocity data (Fig. 7 and Fig. 8b) indicates that the gust front updrafts were composed of environmental air, and that it is the environmental air alone being lifted by the denser, moister GF flow. The maximum vertical velocity associated with GF during the period was only 2.6 ms^{-1}. We speculate that there were two reasons for considerably weak updrafts: AC_{B1} obviously had stabilized the pre-frontal environmental air, before the gust frontal flow forced ambient air to ascend, 2) updraft strength also depends on vertical wind shear of the ambient air. Surface observations and horizontal winds (not

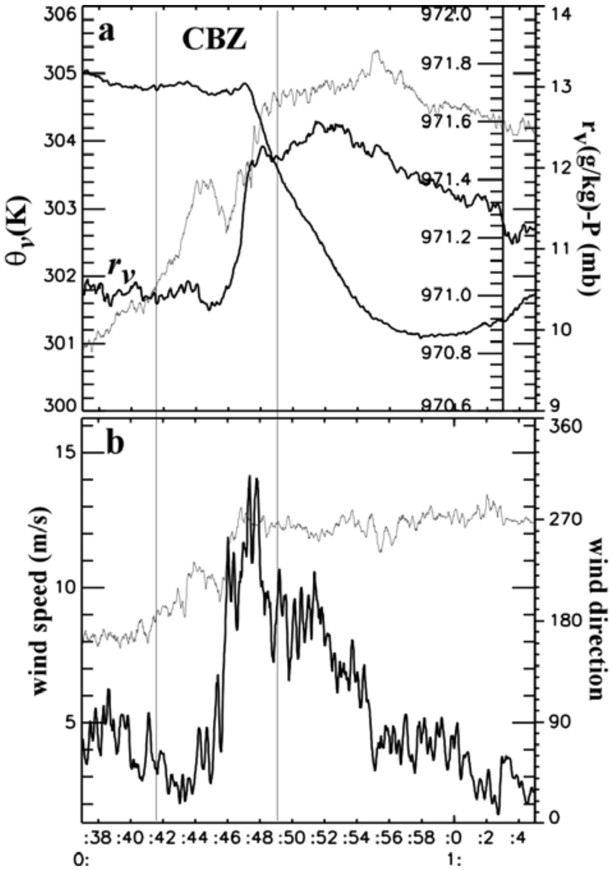

Fig. 7. MIPS surface observations between 0037 and 0105 UTC on June 17 2003. a) time series of virtual potential temperature, mixing ratio, and pressure (grey), b) wind speed and wind direction (grey).

shown) acquired by the profiler and Doppler sodar indicated that southerly ambient flow had no significant contributions to the westerly flow behind the gust front to aid for updraft enhancement.

Negatively buoyant, lifted environmental air descends later on and causes strong downdrafts exceeding -6 m/s aloft. Sudden surface pressure drop after the pressure jump at around 0046 is believed to be manifestation of downdrafts created by the gust front’s inflection points at the interface between the environment and the gust front body. This type of pressure minima behind the gust front head has been observed (e.g., Mueller and Carbone, 87) and suggested by model simulations (e.g., Droegemeier 1987, Sha and Kawamura 1991). Droegemeier (1987) explained it as dynamical effects of the mixed wake behind the gust frontal head. Mueller and Carbone (1987) observed this type of pressure oscillation as well. They observed that small vortices formed at inflections points and associated updrafts/downdrafts.

Vertical velocity variations associated with AC_{B1} between 1.8 km and 4 km have a wave type oscillation. This is also apparent with oscillatory behavior of enhancements in *SNR* (Signal to Noise Ratio) at Fig 8a. Wavy structure of *SNR*

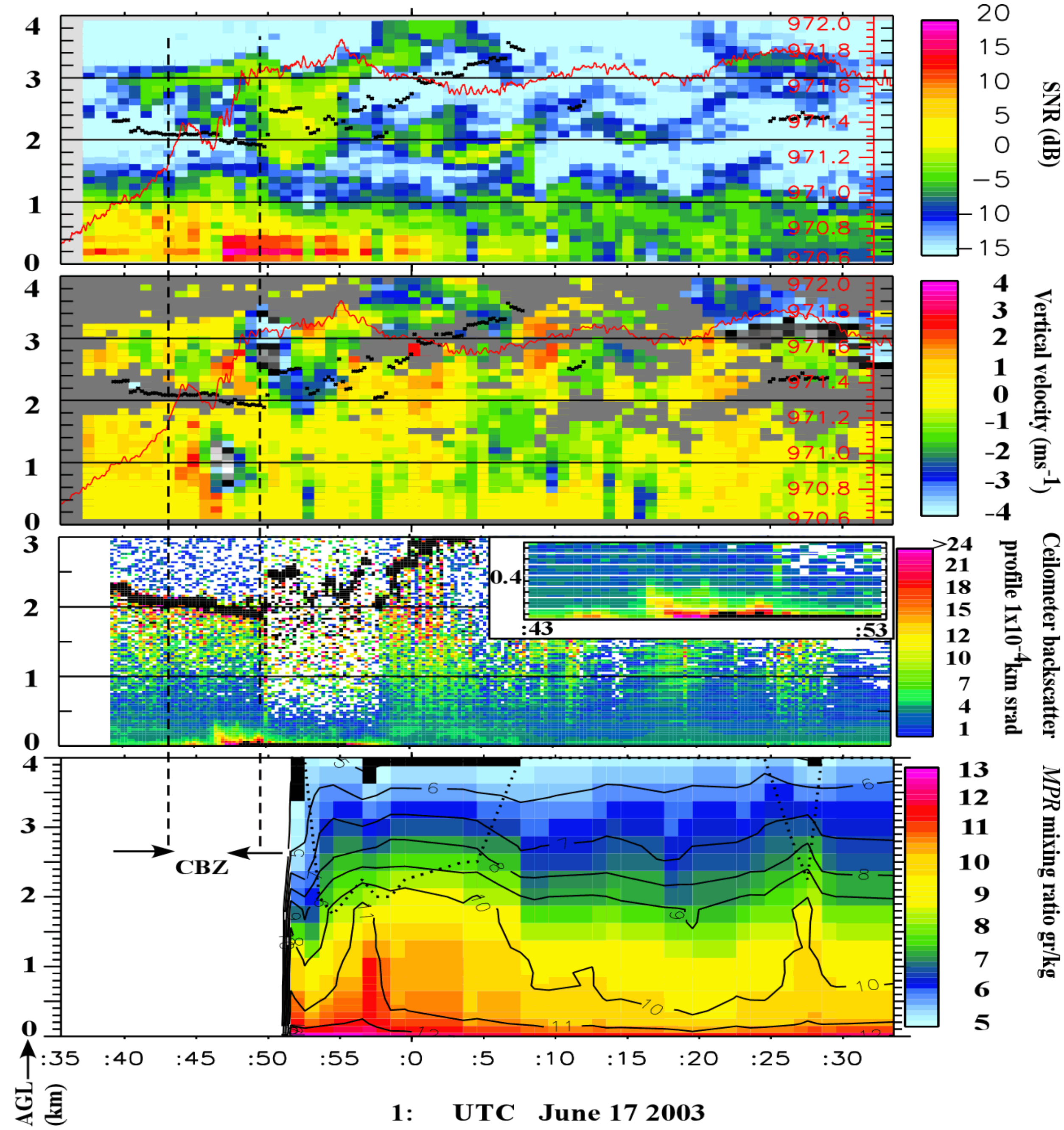

FIG. 8. Time-height section between 0035 and 0134 UTC on June 17 2003: a) 915 MHz profiler Signal-to-Noise ratio, b) mean vertical velocities acquired every 1-minute. Values in black and white colors represent downdrafts exceeding 4 ms^{-1} values. Ceilometer derived cloud base height (black) and surface pressure observations (red) are shown as solid lines at a) and b). c) Ceilometer acquired two-way attenuated backscatter profile. Higher values exceeding the color bar are in black. Blow out plot at the right corner displays ceilometer observations between 0043 and 0053 from surface to 0.7 km. d) time-height observations of water vapor mixing ratio acquired from 12-channel microwave radiometer. MPR requiring warm up time is between 0035 and 0051. Mixing ratio contours are drawn for every 1 g/kg starting at 6 g/kg. CBZ (Convergent Boundary Zone) takes place between 0043 and 0049 UTC.

variations with values between -15 and +3 dB oscillate in a layer between 1.8 km and 4 km. Vertical velocities associated with the wave were about +2 and -3 ms^{-1}. Surface pressure variations of 0.1-0.2 mb were coincident with crests of the wave of the elevated gust front seen at Fig 8a-b. A stable atmospheric layer beneath the anvil of the storm “S” and a more strongly stable shallow layer in the wake of the gust front created favorable conditions for wave energy to be trapped in vertical. Mean vertical velocity maxima associated with GF at 1 km and another maxima associated with AC_{B1} at

2.6 km altitude are in same magnitude (~ 2.7 ms^{-1}). Vertical velocity enhancements associated with AC_{B1} occurred 2 min after the gust frontal updrafts. It is possible that the GF might have formed this gravity wave oscillatory structure at higher elevations. A stable atmosphere at these altitudes is also implied by stronger downward velocities (~ -5 ms^{-1}) than updrafts (~ 2 ms^{-1}). Mean vertical velocity is fluctuated about ±1.5 ms^{-1} along the wave guide with exception that they had the strongest values right after the gust frontal passage at the beginning of the observations.

The ceilometer backscatter profile (Fig. 8c) also indicated aerosol loading starting at 0046 UTC coincident with surface based gust frontal updrafts. A blowup image in Figure 8c suggests that aerosol backscattering was enhanced from surface up to 0.4 km starting at 0046 UTC and ended at the back edge of the *CBZ*. The cloud base height was reduced as the GF approached (from 2.2 km to 1.8 km) and just behind the *CBZ*, the ceilometer indicated reduced cloud cover and increasing cloud base heights. Notice that drier air associated with gust frontal downdrafts is entrained to the lowest 0.5 km few minutes before the end of the *CBZ*. Also, a secondary downdraft region associated with AC_{B1} between 0049 and 0054 UTC at altitudes between 2.0 km and 3.5 km caused another source of subsidence. These unusually strong downdrafts behind the gust frontal head brought drier air into the lower levels as seen at Fig. 8d. The 12-channel radiometer indicated a sudden drop in water vapor associated with gust frontal downdrafts which occurred between 0047-0049 UTC. Unfortunately, at the time of the project microwave radiometer required 10-14 minute warming up process to start the first meaningful observations. Therefore, radiometer observations started few minutes after the *CBZ* passage. But still, it captured some enhancements in water vapor fluctuations within and above the gust frontal body. Based on infrared temperatures of cloud base, radiometer indicated cloud base heights around 2 km between 0055 and 0105 UTC and at 0127 UTC. Integrated water vapor and liquid amount reaches their maximum values at 0055 and 0100 UTC.

4. CONCLUSION

Observations of boundary evolutions and their collisions/interactions studied here have three unique features: 1) head-to-head collision where the collision was very close to the radar. Vertical velocities during the collision time were found to be doubled yet no new cells were initiated close to the collision point. Convergent field derived from the KFSD radial velocities remained shallow occupying the lowest 1 km AGL only. Convective initiation and/or storm enhancement occurred downshear and upshear side of the collision line (Fig. 4c-d). The concept of "stagnation region" instead of stagnation point for computing dynamic pressure was well corroborated with observed dynamic pressure jump associated with gust frontal passage (CBZ). 2) After-collision boundaries exhibited gravity current/wave hybrid structure yet dual finelines associated with one of the after-collision boundaries resembled an atmospheric undular bore. On the other hand, radar derived kinematics and time series of reflectivity field suggested that the secondary vortex was created behind the main gust frontal circulations as the gravity current/wave hybrid propagated into a stable layer. 3) The MIPS sampled two separate weak updrafts associated with surface based gust front and an elevated gust front. Due to strong stability, downdrafts portions of the gust frontal head circulations were significantly greater than updrafts. Ceilometer revealed that interactions between the surface based and elevated gust fronts occurred beneath the storm's anvil.

5. REFERENCES

Benjamin, T. B., 1968: Gravity currents and related phenomena. *J. Fluid Mech.,* **31**, 209-248.

Droegemeier, K. K., R. B. Wilhelmson, 1987: Numerical simulation of thunderstorm outflow dynamics. Part I: Outflow sensitivity experiments and turbulence dynamics. *J. Atmos. Sci.,* **44**, 1180-1210.

Fankhouser, J. C., N. A. Crook, J. Tuttle, L. J. Miller, and C. G. Wade, 1995: Initiation of Deep Convection Along Boundary Layer Convergence Lines in a Semitropical Environment. *Mon. Wea. Rev.,* **123**, 291-313.

Kingsmill, D. E., 1995: Convection Initiation Associated with a Sea-Breeze front a Gust Front, and Their collision. *Mon. Wea. Rev.,* **123**, 2913-2933.

— and N. A. Crook, 2003: An observational study of atmospheric bore formation from colliding density currents. *Mon. Wea. Rev.,* **131**, 2985-3002.

Mueller, C. K. and R. E. Carbone, 1987: Dynamics of a thunderstorm outflow. *J. Atmos. Sci.,* **44**, 1879-1898.

Sha, W. and T. Kawamura, 1991: A Numerical Study on Sea/Land Breezes as a Gravity Current: Kelvin-Helmholtz Billows and Inland Penetration of the Sea-Breeze Front. *J. Atmos. Sci.*, **48**, 1648-1665.

Simpson, J. E. and R. E. Britter, 1980: A Laboratory Model of an Atmospheric Mesofront. *Quart. J. R. Met. Soc.,* **106**, 485-500.

Wakimoto, R. M. and D. E. Kingsmill, 1995: Structure of an Atmospheric Undular Bore Generated from Colliding Boundaries during CaPE. *Mon. Wea. Rev.,* **123**, 1374-1392.

Wilson, J. W. and W. E. Schreiber, 1986: Initiation of convective storms at radar-observed boundary-layer convergence lines. *Mon. Wea. Rev.,* **114**, 2516-2536.

Xue, M, 2002: Density Currents in Shear Flows: Effects of Rigid lid and Cold-Pool Internal Circulation, and Application to Squall Line Dynamics. *Quart. J. R. Met. Soc.*, **128**, 47-73.